BRNO UNIVERSITY OF TECHNOLOGY
VYSOKÉ UČENÍ TECHNICKÉ V BRNĚ

FACULTY OF ELECTRICAL ENGINEERING AND COMMUNICATION
FAKULTA ELEKTROTECHNIKY A KOMUNIKAČNÍCH TECHNOLOGIÍ

DEPARTMENT OF RADIO ELECTRONICS
ÚSTAV RADIOELEKTRONIKY

MILLIMETER WAVE BAND WIRELESS CHANNEL MEASUREMENT TECHNIQUES IN AUTOMOTIVE APPLICATIONS
METODY MĚŘENÍ PŘENOSOVÝCH KANÁLŮ V PÁSMU MILIMETROVÝCH VLN V OBLASTI AUTOMOBILOVÝCH APLIKACÍ

SHORT VERSION OF DOCTORAL THESIS
TEZE DIZERTAČNÍ PRÁCE

AUTHOR
AUTOR PRÁCE
Ing. Josef Vychodil

ADVISOR
VEDOUCÍ PRÁCE
Dr. Techn. Vojtěch Derbek

BRNO 2021

CONTENTS

Introduction **3**

1 Channel measurement methods **3**

1.1 Channel sounding in the time domain 3

1.2 Channel sounding in the frequency domain 4

1.3 Interpreting the channel measurements results 5

1.4 Other MMW time domain channel sounding systems 6

2 Aims of the dissertation **7**

3 Millimeter Wave Band Time Domain Channel Sounder **8**

3.1 System description 8

3.2 Definitions 10

3.2.1 Cross-correlation function 10

3.2.2 Autocorrelation function 10

3.2.3 Higher order autocorrelation function 11

3.2.4 Ambiguity function 12

3.3 Basic principle of operation 13

3.4 Operation in the presence of non-linearities 14

3.4.1 Unobservable and overlapped kernels 20

3.4.2 Mitigating the effects of even order kernels 20

3.4.3 Golay complementary sequences as an input signal 20

3.4.4 Non-inverted and inverted Golay complementary sequences as an input signal 22

3.5 Probing the system with multiple sequences 23

3.6 SFDR of the system 24

3.6.1 SFDR of the baseband system 24

3.6.2 SFDR of the system without PA and LNA 25

3.6.3 SFDR of the complete system (including PA and LNA) 27

3.7 IQ imbalance 28

3.7.1 IQ imbalance compensation 29

4 Conclusion **32**

Bibliography **33**

INTRODUCTION

The growing demand for fast, reliable and low latency wireless communication lead to enormous improvements in the modulation, encoding and other physical layer techniques in the last few decades. However, even using those techniques, it is impossible to fulfil the extreme requirements — for example data rates in the order of tens of gigabits per second and latency less than one millisecond — for the next generation wireless systems within the limited bandwidth of the conventional sub-6 GHz band.

There are several frequency bands, with huge available bandwidth, which can be utilized for those next generation systems. One of the most promising is the Millimeter Wave Band (MMW), namely 30–300 GHz, which is relatively unused nowadays and ready for future systems deployment.

Besides "classical", for example fixed (WiFi) or mobile (Long Term Evolution (LTE)) communication systems, there is a whole new emerging field, which will take an advantage of those new systems — the self-driving car industry. To ensure the safety and reliability of this transportation, a robust communication between the nodes (either the vehicles or some infrastructure structures) is needed. Additionally, to provide comfort and entertainment to the crew during the journey, a broadband connectivity inside the vehicle is of high advantage.

In order to make development of those systems possible, one of the most important topics to understand is the knowledge of the environment's electromagnetic wave propagation characteristics. This thesis addresses the problem of obtaining these parameters.

1 CHANNEL MEASUREMENT METHODS

The parameters of the radio channel may be obtained through a process called channel sounding. There are several techniques and methods that can be utilized to perform those measurements. Basically, the channel sounding methods can be divided into those working in the time domain and those operating in the frequency domain.

1.1 Channel sounding in the time domain

The most obvious and straightforward method of performing a channel measurement in the time domain is to transmit an ideal (e.g. Dirac) pulses and receive the response by a sampling device, for example the oscilloscope. This is of course unfeasible to be done in reality — there is a number of practical limitations. However, one can transmit band limited pulses which approach the ideal Dirac pulse in several properties.

In [1, 2], our team has presented a time domain channel sounding by transmitting Gaussian pulses (or its derivatives) and then recovering the Channel Impulse Response (CIR) by deconvolving the received signal utilizing the CLEAN algorithm. However this approach is challenging for the power amplifiers and provides low Signal to Noise Ratio (SNR).

Utilizing pulse sequences rather than single pulse provides substantial improvement in various system parameters — it for example relaxes the requirements for the power amplifier by reducing the Peak to Average Power Ratio (PAPR) and also improves the SNR by exploiting the correlation gain. For example, authors of [3, 4, 5, 6] presented numerous practical channel measurements by transmitting and receiving wideband pulse sequences.

Several papers deal with the design of the time domain channel sounder for the 60 GHz band; usually utilizing custom hardware design or even custom silicon chips, whose development is very time consuming. For example, authors of [7] propose a sounding system with a bandwidth of 100 MHz without the need of a cabled connection between the transmitter and receiver, thus enabling flexible measurements. Purely hardware designs of channel sounders often use the so-called sliding correlator technique for data processing, as was shown, for example in [8]. Other papers, e.g. [9] or [10], describe various multiple input multiple output (MIMO) time domain channel sounding systems with a bandwidth of several GHz and a reasonable dynamic range of 30–50 dB.

To summarize, channel sounders operating in the time domain usually provide fast measurements speeds (e.g. several tens of thousands measurements per seconds), flexibility (separated transmit and receive parts of the system), but on the other hand suffer from poor dynamic range.

1.2 Channel sounding in the frequency domain

Measurements in the frequency domain are conventionally carried out using a Vector Network Analyzers (VNAs), which perform stepped frequency sweeping as it was shown, for example, in [11, 12, 13, 14, 15]. It is easily conducted by utilizing off-the-shelf laboratory instruments and offers excellent dynamic range usually greater than 60 dB. On the other hand — a complete sweep over the frequency range of interest using VNA usually takes several tens of seconds, depending on the number of frequency steps and requested dynamic range. During this time, the channel must remain static. For this reason, the VNA method cannot be used to measure either slowly changing channels (caused e.g. by people or vehicle movement) or for measuring fast changing channels (caused e.g. by vibrations). Another great disadvantage of this technique is the fact that the transmitter and receiver is physically one device, which limits the use to static indoor, small range outdoor or intra car channels, but forbid deployment in the Vehicle to Vehicle (V2V) or Vehicle to Infrastructure (V2I) environments.

Another approach, which could be considered as a frequency domain method, is utilizing a multi-tone waveform as an excitation signal. For example, in [16], authors presented a flexible channel sounding system of this type. An Arbitrary Waveform Generator (AWG) is used as a transmitter, which offers several advantages such as flat frequency spectrum, controllable crest factor or high SNR through processing gain. However, even with a modern AWG, the

system bandwidth is in this case limited to 500 MHz.

1.3 Interpreting the channel measurements results

Depending on which of the methods mentioned in previous paragraphs was used, some sort of post processing of the obtained data is needed to obtain useful results.

When the direct time domain RF pulse approach is used, then the recorded data is instantly an approximation of the CIR, which happens to be a standard convenient way of how to deterministically represent a single channel realization characteristics. It shows the channel output when the input is a Dirac impulse. The general way to model a CIR of a time invariant multipath wireless channel is to express it as a sum of attenuated, delayed and phase shifted replicas of the Dirac delta function:

$$h(t) = \sum_{n=0}^{L-1} \rho_n e^{j\Phi_n} \delta(t - \tau_n), \tag{1.1}$$

where L is the number of multipath components, δ is the Dirac delta function and τ_n, ρ_n and Φ_n is the path delay, gain and phase shift of n-th component, respectively.

Measurements in the time domain using pulse sequences usually requires post processing by means of correlating the received signal with the transmitted replica, e.g. matched filtering in order to obtain the CIR estimation.

The measurements in the frequency domain using VNA provides the Channel Transfer Function (CTF) $H(f)$ in terms of the s parameter, which represents the channel gain and phase shift as a function of frequency. We can exchange without any loss of information between the $H(f)$ and the $h(t)$ representation utilizing Fast Fourier Transform (FFT) or more precisely Inverse Fast Fourier Transform (IFFT):

$$\begin{aligned} H(f) &= \int_{-\infty}^{\infty} h(t) e^{-j2\pi f t} dt \\ &= \sum_{n=0}^{L-1} \rho_n e^{j\Phi_n} e^{-j2\pi f \tau_n}. \end{aligned} \tag{1.2}$$

The post processing of the measured VNA data usually consists of two steps — multiplying $H(f)$ by a windowing function (e.g. Hann) to mitigate the leakage effects and then applying the IFFT to get the CIR $h(t)$.

The CIR is of interest for several reasons. First of all, it contains all the information needed to extract any of the channel parameters, for example the path loss, propagation delay, power delay profile, delay spread or coherence bandwidth. When the evolution of the CIR in time is captured, it contains an additional information about the channel such as Doppler spread or if slow fading or shadowing occurs. One can also determine e.g. the transmitter and receiver relative velocities as well as distances and velocities of any objects involved in the particular

channel layout. When various channel realisations (with their evolution in time) are captured in different places and scenarios, a statistical model can be created based upon that data. That model then can be used to generate arbitrary large number of different CIRs (corresponding to the given environment) to help the development and evaluation of the device or system under development.

1.4 Other MMW time domain channel sounding systems

After carefully considering all of the above mentioned channel sounding system designs, evaluating their pros and cons and taking into account all of the requirements (which are specified and explained in Chapter 2), a time domain system based on pulse sequences was chosen as a system design for this thesis.

Table 1.1 [17] lists other similar time domain channel sounding systems working in the MMW and their basic parameters.

Reference	Institution	Sounder type	Measurement parameters
[18]	NYU-1	Sliding correlation	1 GHz bandwidth up to 30500 snapshots/s
[19]	UT Austin	Sliding correlation	1.5 GHz bandwidth stationary measurements
[20]	Virgina Tech	Sliding correlation	0.8 GHz bandwidth stationary measurements
[21]	ESTG	Sliding correlation	2 GHz bandwidth 2000 snapshots/s
[22]	University of VIGO	Sliding correlation	0.5 GHz bandwidth stationary measurements
[23]	Ilmenau-01	M-sequence direct correlation	7 GHz bandwidth 200 snapshots/s
This work	Brno University of Technology	Golay sequence direct correlation	8 GHz bandwidth up to 700000 snapshots/s

Tab. 1.1: Channel sounder systems list.

2 AIMS OF THE DISSERTATION

Based on previous chapters, it is obvious that the current available methods for channel measurements are not capable to capture all of the millimeter wave band channel features. The combination of huge bandwidth, fast channel variations and great dynamic range makes it very challenging. The *primary* goal of this thesis is therefore to design and build a channel sounding system, which will be optimized for measuring those complicated channels. The requirements for this system are following:

- It will be predominately made of off-the-shelf components because various instruments are already available at the author's university.
- The transmitting and receiving parts should be separated to enable various measurement scenarios.
- The band of the interest will be the MMW, e.g. ~55–65 GHz because it is (at least partially) available for unlicensed use.
- The captured bandwidth should be at least in order of several GHz to enable close multipath components separation.
- The measurement rate should reach several thousand or tens of thousands measurements per second in order to unambiguously measure channels with Doppler spread up to several kHz.
- The dynamic range of the system shall top off about 40–50 dB so even weak multipath components can be identified. It also eases measurements of some scenarios where the received power varies rapidly, e.g. cars approaching towards each other.

The *secondary* goal is to perform actual measurements with the developed system. The scenarios could be following:

- Measurements of the channel inside a single vehicle (intra-car channel).
- Measurements of the V2V channel.
- Measurements of the V2I channel.

The steps, which will ultimately lead to achieve those goals, could be as follows:

- Develop a basic concept of the channel sounding system with transmitting and receiving parts sharing the same time reference and physical place. This will enable at least the intra-car channel measurements and will reveal where to focus on the improvements in terms of e.g. the dynamic range.
- Upgrade the system by splitting the transmit and receive parts. This will enable all measurement scenarios, including the V2V and V2I channels, but on the other hand, brings challenges like synchronization and triggering issues.

3 MILLIMETER WAVE BAND TIME DOMAIN CHANNEL SOUNDER

This chapter is based on the following published paper:

J. Vychodil, M. Pospíšil, A. Prokeš, and J. Blumenstein, "Millimetre wave band time domain channel sounder," *IET Communications*, vol. 13, no. 3, pp. 331–338, January 2019.

Author of this thesis contribution

All of the work, presented in this chapter, including the measurement setup architecture, data processing concept, system performance and probing signal analysis, and IQ imbalance compensation, was done entirely by the author of this thesis with little help and consultation with the co-authors.

3.1 System description

A simplified block diagram of the proposed channel sounding system is depicted in Fig. 3.1. An Anritsu Signal Quality Analyzer MP1800A serves as a baseband binary sequence generator at data rates up to $f_{\text{chip}} = 12.5$ Gbits/s with maximum RF output power of 13 dBm. A Tektronix Digital Sampling Oscilloscope MSO72004C is utilized as a receiver. It provides 4 channels, 16 GHz bandwidth, 50 GS/s real time acquisition rate and 31.25 MS of data storage per channel. The Signal Quality Analyzer also provides 10 MHz reference and a gating (triggering) signal to the oscilloscope. The Power Amplifier (PA) and Low Noise Amplifier (LNA) (not depicted) are the QuinStar QPW-50662330 and QLW-50754530-I2 respectively. A PC can be used to control the instruments, interchange data and to provide additional features (e.g. real-time and continuous channel sounding), but is not necessary for the data acquisition.

The Sivers IMA FC1003V/01 [24] up-down converter is used for frequency shifts between the baseband and the radio frequency. It is a direct conversion transceiver (sometimes called homodyne or zero-IF) with IF input bandwidth up to 5 GHz. The transmitted baseband signal is filtered by a low pass filter with cut off frequency of 5 GHz and then fed into the I branch of the up converter. The Q branch is terminated by a $50\,\Omega$ termination load. In an ideal case this results in an Amplitude Modulation (AM) with a symmetrical spectrum around the carrier frequency $f_c = 59.6$ GHz. The RF signal then propagates through the channel, which is the object of the measurement. For the channel sounding, typically an open ended WR15 waveguide is used, as it is very simple and it offers an acceptable radiation pattern [25]. The received signal is then down converted and the output signal — complex, in the form of I and Q components — is passed to the oscilloscope for sampling and further processing. To achieve perfect coherency the Local Oscillator (LO) signal is generated in an Agilent RF generator 83752A then it is split in the Wilkinson power divider and fed into the up-down

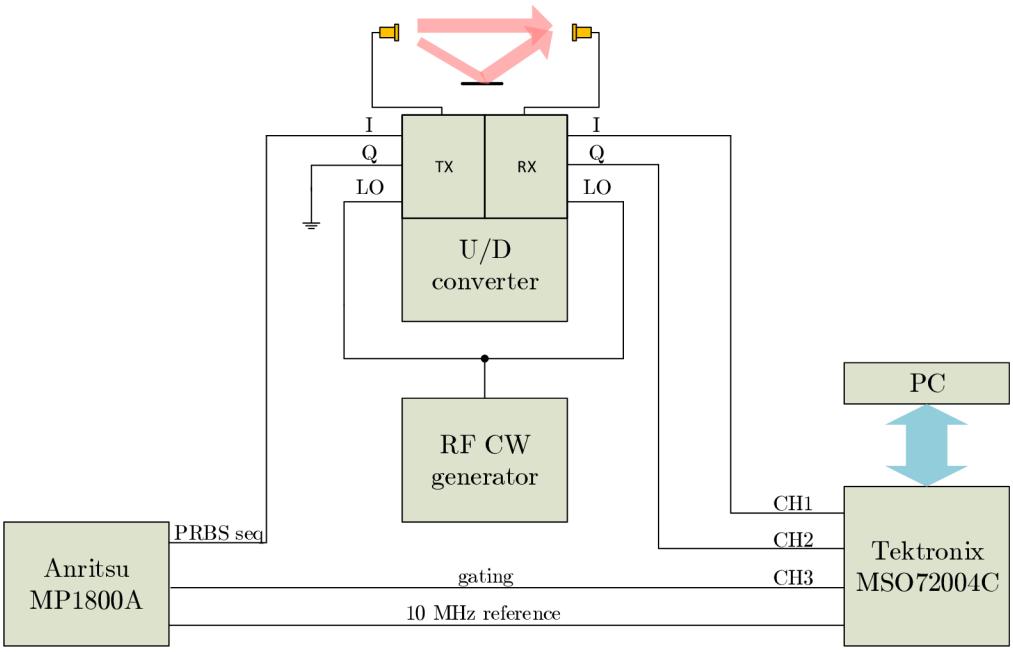

Fig. 3.1: Proposed MMW channel sounder architecture.

converter LO inputs. Alternatively, the Sivers IMA FC1005V/00 [26] up-down converter can be used. This converter contains two PLL synthesizers, but due to their large group delay variation (1 ns/GHz), they have to be disconnected and replaced by a power splitter and a more stable RF generator, e.g. the aforementioned Agilent 83752A.

In our case, a seamless repeating binary sequence is used as the excitation signal. The length of the binary sequence is N chips. The number of chips determines the time period of the sequence, which corresponds to the maximum observable CIR time span given by

$$T = \frac{N}{f_{\text{chip}}} = N \cdot \Delta t, \tag{3.1}$$

where $\Delta t = \frac{1}{f_{\text{chip}}}$ is the time duration of one chip. The parameter T is related to the maximum observable propagation distance by

$$D_{\max} = c \cdot T = c \cdot \frac{N}{f_{\text{chip}}} = c \cdot N \cdot \Delta t, \tag{3.2}$$

where $c \approx 3 \times 10^8\,\mathrm{m\,s^{-1}}$ is the speed of light. Considering $N \approx 2^{11} = 2048$ and $f_{\text{chip}} = 12.5$ GHz, the maximum propagation distance is $D_{\max} \approx 49$ m, which is sufficient for most of the short-range MMW channels.

Correlation gain, which can be viewed as simple averaging of N equivalent samples with additive white Gaussian noise, is given by [27]

$$G_{\text{corr}} = 10 \cdot \log N, \tag{3.3}$$

when considering the probing sequence as perfect or almost perfect. This property is discussed in Sec. 3.2.2. For example, if $N = 2048$, the correlation gain is $G_{\text{corr}} = 33.11$ dB.

The main advantage of the proposed channel measurement system is the CIR measurement time. The time to measure one single CIR equals the time length of the sequence given by Eq. (3.1). Considering $N = 2048$, this leads to $T = 0.164\,\mu\text{s}$. The reciprocal value, $f_{\text{meas}} = \frac{1}{T}$ denotes the maximum CIR measurements per second. For $N = 2048$, this is theoretically 6.1 million measurements per second. The oscilloscope provides 31.25 MS of fast acquisition memory per channel, which equals to 0.625 ms at a sampling rate of 50 GS/s, so only 3816 CIRs can be captured at once. Nevertheless, using advanced triggering modes, the f_{meas} can be decreased to an arbitrary value. It is also possible to continuously stream the real time acquired data to a PC at the rate $f_{\text{meas}} \approx 100$ Hz. In static channel measurement scenarios, averaging of the data can be utilized to further improve the SNR.

3.2 Definitions

Several terms, which will be used in this chapter, are defined in this section.

3.2.1 Cross-correlation function

The cross-correlation between two complex valued functions $a(t)$ and $b(t)$ can be defined as

$$R_{ab}(\tau_1) = \int_{-\infty}^{\infty} a(t)b^*(t-\tau_1)\mathrm{d}t, \tag{3.4}$$

where * denotes complex conjugation. When considering $a(t)$ and $b(t)$ periodic with period T, the cross-correlation can be defined as

$$R_{ab}(\tau_1) = \frac{1}{T}\int_{0}^{T} a(t)b^*(t-\tau_1)\mathrm{d}t = \overline{a(t)b^*(t-\tau_1)}, \tag{3.5}$$

where $\overline{}$ means time (t) average over one period (T) of the signal. The cross-correlation is often performed utilizing the Fourier transform for faster calculation as

$$\hat{R}_{ab}(f_1) = \hat{a}(f_1)[\hat{b}(f_1)]^*, \tag{3.6}$$

where $\hat{}$ denotes the Fourier transform, i.e. $\hat{a}(f_1) = \mathcal{F}\{a(\tau_1)\}$.

3.2.2 Autocorrelation function

The autocorrelation function of the signal $a(t)$ can be obtained from Eq. 3.4 by letting $b(t) = a(t)$. If the signal $a(t)$ is periodic with period T, the autocorrelation function can be obtained in the same way from Eq. 3.5. Because this work is focused on periodic binary (e.g. real

valued) sequences, it will be more convenient to examine the discrete time periodic (circular) autocorrelation function

$$R_{aa}[\tau_1] = \frac{1}{N}\sum_{n=0}^{N-1} a[n]a[n-\tau_1], \tag{3.7}$$

where N is the number of chips of sequence $a[n]$ and the indexes are computed via the modulo N operation, e.g. $a[n] \equiv a[n \bmod N]$. The ideal shape of $R_{aa}[\tau_1]$, suitable for the purposes of channel sounding, is the unit impulse,

$$R_{aa}[\tau_1] = \begin{cases} 1 & \text{if } \tau_1 = 0 \\ 0 & \text{elsewhere.} \end{cases} \tag{3.8}$$

Signals with this property are called perfect. If a signal with this property is transformed into continuous time digital signal with chip period Δt, the corresponding $R_{aa}(\tau_1)$ is a triangle shaped signal with its base spanning from $-\Delta t$ to Δt and height 1. Given a band limited function $s(t)$ with bandwidth $B \ll \frac{1}{\Delta t}$, it can be approximated

$$\int_{-\Delta t}^{\Delta t} s(\tau_1)R_{aa}(\tau_1)\mathrm{d}\tau_1 \approx \Delta t \cdot s(0). \tag{3.9}$$

3.2.3 Higher order autocorrelation function

If we consider the signal $a(t)$ as real and $b(t) = a(t)$, we can write Eq. 3.4 as

$$R_{aa}(\tau_1) = \int_{-\infty}^{\infty} a(t)a(t-\tau_1)\mathrm{d}t. \tag{3.10}$$

This (first order) autocorrelation function (of a real valued signal) can be extended to the i-th order autocorrelation function as

$$R_{a\ldots a}(\tau_1, \ldots, \tau_i) = \int_{-\infty}^{\infty} a(t)a(t-\tau_1)\ldots a(t-\tau_i)\mathrm{d}t. \tag{3.11}$$

Please note that the i-th order autocorrelation function is symmetric, meaning that its value is the same for any permutation of input parameters, for example $R_{aaa}(\tau_1, \tau_2) = R_{aaa}(\tau_2, \tau_1)$ or $R_{aaaa}(\tau_1, \tau_2, \tau_3) = R_{aaaa}(\tau_1, \tau_3, \tau_2) = R_{aaaa}(\tau_2, \tau_1, \tau_3) = R_{aaaa}(\tau_2, \tau_3, \tau_1) = R_{aaaa}(\tau_3, \tau_1, \tau_2) = R_{aaaa}(\tau_3, \tau_2, \tau_1)$ and so on. Similarly as in Eq. 3.5, it is possible to write a higher order autocorrelation function of a periodic signal as

$$\begin{aligned} R_{a\ldots a}(\tau_1, \ldots, \tau_i) &= \frac{1}{T}\int_{0}^{T} a(t)a(t-\tau_1)\ldots a(t-\tau_i)\mathrm{d}t \\ &= \overline{a(t)a(t-\tau_1)\ldots a(t-\tau_i)}. \end{aligned} \tag{3.12}$$

Similarly, as in Eq. 3.7, it is possible to write a discrete time higher order autocorrelation function as

$$R_{a\ldots a}[\tau_1, \ldots, \tau_i] = \frac{1}{N} \sum_{n=0}^{N-1} a[n]a[n-\tau_1] \ldots a[n-\tau_i]. \tag{3.13}$$

Considering $R_{a\ldots a}[\tau_1, \ldots, \tau_i]$ i-dimensional unit impulse, e.g.

$$R_{a\ldots a}[\tau_1, \ldots, \tau_i] = \begin{cases} 1 & \text{if } \tau_1 = \cdots = \tau_i = 0 \\ 0 & \text{elsewhere,} \end{cases} \tag{3.14}$$

for the corresponding $R_{a\ldots a}(\tau_1, \ldots, \tau_i)$ given band limited function $s(t_1, \ldots, t_i)$ with bandwidth $B \ll \frac{1}{\Delta t}$, it can be approximated

$$\begin{aligned} &\int_{-\Delta t}^{\Delta t} \cdots \int_{-\Delta t}^{\Delta t} s(t_1, \ldots, t_i) \\ &R_{a\ldots a}(\tau_1, \ldots, \tau_i) \mathrm{d}\tau_1 \ldots \mathrm{d}\tau_i \approx (\Delta t)^i \cdot s(0, \ldots, 0) \end{aligned} \tag{3.15}$$

as a generalization of Eq. 3.9.

The higher order autocorrelation function can also be computed utilizing the Fourier transform as [28]

$$\hat{R}_{a\ldots a}(f_1, \ldots, f_i) = \hat{a}(f_1)\hat{a}(f_2) \ldots \hat{a}(f_i)[\hat{a}(f_1 + f_2 + \cdots + f_i)]^*, \tag{3.16}$$

where $\hat{}$ denotes the i-dimensional Fourier transform, i.e. $\hat{a}(f_1, \ldots, f_i) = \mathcal{F}\{a(\tau_1, \ldots, \tau_i)\}$.

It will be shown later in this thesis that the higher order autocorrelation function can be used to characterize the measurement output when the channel (or the system) under test exhibits non-linear behavior.

3.2.4 Ambiguity function

The (narrowband) ambiguity function of signal $a(t)$, often used in radar signal processing, can be defined as [29]

$$\chi(\tau_1, f) = \int_{-\infty}^{\infty} a(t)a^*(t-\tau_1)e^{i2\pi ft} dt, \tag{3.17}$$

where i is the imaginary unit and f is the Doppler frequency shift. It basically shows the change of the shape of the autocorrelation function caused by the relative movement of the transmitter and receiver (the Doppler effect). Due to relatively low transmitter and receiver relative speeds (maximum tens or hundreds of $\mathrm{m\,s^{-1}}$), huge bandwidth and very short measurement times in our scenario, the Doppler effect affecting single measurement is negligible. The slice at $f = 0$ of the ambiguity function is the autocorrelation function, i.e.

$$\chi(\tau_1, 0) = R_{aa}(\tau_1). \tag{3.18}$$

3.3 Basic principle of operation

The measured channel can be modeled as a linear time invariant system whose input-output relationship can be expressed as

$$y(t) = \int_{-\infty}^{\infty} g_1(\tau_1)u(t-\tau_1)\mathrm{d}\tau_1, \tag{3.19}$$

where $u(t)$ is the input of the system, $y(t)$ is its output and $g_1(\tau_1)$ is the channel impulse response.

There are many types of excitation signals which can be utilized in order to perform channel sounding. One can use, for example, frequency sweeps (chirps), binary sequences or some more complicated signals, e.g. Orthogonal Frequency Division Multiplex (OFDM)-like signals or Zadoff-Chu sequences [30]. This work focuses on the use of the binary sequences signal group because they are easily generated and modulated to the desired frequency band using inexpensive hardware.

In the scope of this work, the two types of binary signals are examined — the Maximum Length Sequences (MLSs), sometimes called m-sequences and Golay complementary pairs. As was stated earlier, the signal $u(t)$ is a seamless repeating sequence with the number of chips N, period of T and duration of one chip Δt. Since it is assumed that the $g_1(\tau_1)$ is causal and has a finite length of T, i.e.

$$g_1(\tau_1) = 0 \text{ for } \tau_1 > T \text{ and } \tau_1 < 0, \tag{3.20}$$

and the input signal $u(t)$ is periodic with period T, Eq. 3.19 can be rewritten as

$$y(t) = \int_{0}^{T} g_1(\tau_1)u(t-\tau_1)\mathrm{d}\tau_1. \tag{3.21}$$

The m-sequence cross-correlation method is a widely used approach for measuring impulse responses of linear systems. For example, it is used in many time domain channel sounders, like it was shown in [9] or [5]. M-sequences have several properties which makes them appropriate for channel sounding. They are easily generated by the Linear Feedback Shift Register (LFSR) and have an almost perfect circular autocorrelation function

$$R_{uu}[\tau_1] = \begin{cases} 1 & \text{if } \tau_1 = 0 \\ -\frac{1}{N} & \text{elsewhere.} \end{cases} \tag{3.22}$$

An example of a circular autocorrelation function of a short m-sequence is depicted in Fig. 3.2.

The cross-correlation between the output $y(t)$ and input $u(t)$ can be expressed using Eq. 3.5 as [31]

$$R_{yu}(\tau) = \overline{u(t-\tau)y(t)}, \tag{3.23}$$

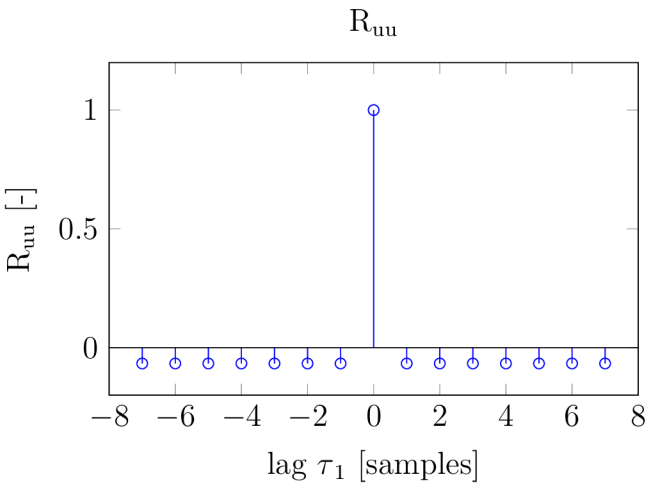

Fig. 3.2: Circular autocorrelation function of a m-sequence.

where $\overline{}$ means time (t) average over one period (T) of the signal. When considering the system described by Eq. 3.21, the cross-correlation becomes

$$\begin{aligned} R_{yu}(\tau) =& \overline{u(t-\tau)y(t)} \\ =& \overline{u(t-\tau)\int_0^T g_1(\tau_1)u(t-\tau_1)\mathrm{d}\tau_1} \\ =& \int_0^T g_1(\tau_1)\overline{u(t-\tau)u(t-\tau_1)}\mathrm{d}\tau_1 \\ =& \int_0^T g_1(\tau_1)\overline{u(t)u(t-\tau_1+\tau)}\mathrm{d}\tau_1 \\ =& \int_0^T g_1(\tau_1)R_{uu}(\tau_1-\tau)\mathrm{d}\tau_1, \end{aligned} \tag{3.24}$$

where $R_{uu}(\tau)$ is the autocorrelation function of the input sequence $u(t)$. Using Eq. 3.9 or 3.15, Eq. 3.24 then becomes

$$R_{yu}(\tau) \approx \Delta t \cdot g_1(\tau), \tag{3.25}$$

which is an estimate of the measured CIR.

3.4 Operation in the presence of non-linearities

Real-world (and not only) electronic devices like amplifiers, mixers, etc., used in the measurement chain, exhibit at least weak non-linear behavior. When the measured system is non-linear, the resulting estimate of the channel impulse response contains artefacts, which are not part of the linear impulse response. An example of a measurement result using the

proposed system and the m-sequence is shown in Fig. 3.3 (a). The measurement is done only in the baseband, e.g. the up-down converter is not used and the output of the generator is connected directly into one channel of the oscilloscope using a coaxial cable. Several thousands of measurements are averaged to improve the SNR in order to provide a better demonstration. It is possible to see the direct path located at roughly 15 ns and also some spurious peaks located at 8 ns and 110 ns, which are caused by the non-linearities. Please note that there are other components besides the main path which are caused by the low pass filter behavior of the coaxial cable and by the reflections. However, those components are fundamentally linear and thus can be easily removed by means of calibration or normalization.

The metric used in the scope of this thesis for comparing the performance of different systems or sequences is the Spurious-Free Dynamic Range (SFDR). It is the ratio of the strongest wanted component and the strongest spurious or noise component. The SFDR is also shown graphically in Fig. 3.3.

When the system is weakly non-linear, its input-output relation can be expressed using the Volterra series expansion, which is a generalization of the system impulse response and the Taylor series, as

$$\begin{aligned} y(t) &= \int_0^T g_1(\tau_1)u(t-\tau_1)\mathrm{d}\tau_1 \\ &+ \int_0^T\int_0^T g_2(\tau_1,\tau_2)u(t-\tau_1)u(t-\tau_2)\mathrm{d}\tau_1\mathrm{d}\tau_2 \\ &+ \int_0^T\int_0^T\int_0^T g_3(\tau_1,\tau_2,\tau_3)u(t-\tau_1)u(t-\tau_2)u(t-\tau_3)\mathrm{d}\tau_1\mathrm{d}\tau_2\mathrm{d}\tau_3 \\ &+ \dots \\ &+ \int_0^T\dots\int_0^T g_i(\tau_1,\dots,\tau_i)u(t-\tau_1)\dots u(t-\tau_i)\mathrm{d}\tau_1\dots\mathrm{d}\tau_i \end{aligned} \tag{3.26}$$

or in shorter form as

$$y(t) = \sum_{i=1}^{\infty}\int_0^T\dots\int_0^T g_i(\tau_1,\dots,\tau_i)u(t-\tau_1)\dots u(t-\tau_i)\mathrm{d}\tau_1\dots\mathrm{d}\tau_i, \tag{3.27}$$

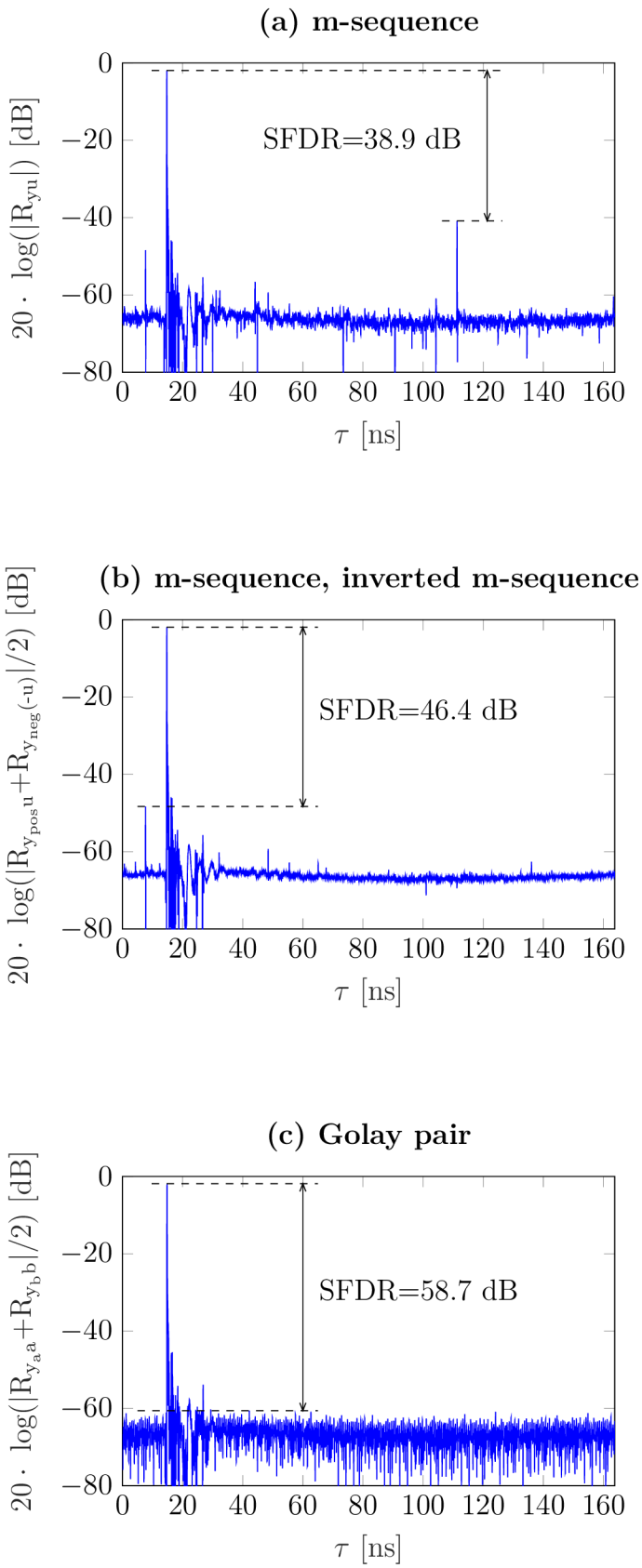

Fig. 3.3: Example of baseband back-to-back measurement using different sequences. (a) m-sequence; (b) m-sequence, inverted m-sequence; (c) Golay pair.

where $u(t)$ is the input to the system, $y(t)$ is the output of the system and $g_i(\tau_1, \ldots, \tau_i)$ is the i-th order Volterra kernel, which can be viewed as a higher order impulse response of the system. Please note that if the system is linear, only the first order Volterra kernel $g_1(\tau_1)$ (first term of Eq. 3.26) is non zero. The equation then reduces to an ordinary convolution, where $g_1(\tau_1)$ is the linear impulse response, e.g. the equation becomes Eq. 3.19.

To provide an example, consider one of the simplest non-linear systems, the so-called Wiener model. This model consists of a cascade of a linear memory block which can be characterized by its impulse response $h(\tau)$ and a static (memory-less) non-linearity which can be modeled by a (possibly truncated) polynomial, e.g.

$$y(t) = c_1 z(t) + c_2 z^2(t) + c_3 z^3(t), \tag{3.28}$$

when considering non-linearities only up to the third order. The i-th order Volterra kernel of this system is then [32]

$$g_i(\tau_1, \ldots, \tau_i) = c_i h(\tau_1) \ldots h(\tau_i). \tag{3.29}$$

This model is mentioned here only to provide a better insight into how the Volterra kernels can appear in practice. The principles described in this thesis apply to the general Volterra model, defined above in Eq. 3.27.

The cross-correlation between the the output $y(t)$ and input $u(t)$ using Equations 3.12, 3.27 and 3.23 can be rewritten as [33]

$$\begin{aligned} R_{yu}(\tau) =& \overline{u(t-\tau)y(t)} \\ =& \overline{u(t-\tau)\sum_{i=1}^{\infty}\int_0^T \ldots \int_0^T g_i(\tau_1, \ldots, \tau_i) \cdot u(t-\tau_1) \ldots u(t-\tau_i) \mathrm{d}\tau_1 \ldots \mathrm{d}\tau_i} \\ =& \sum_{i=1}^{\infty}\int_0^T \ldots \int_0^T g_i(\tau_1, \ldots, \tau_i) \cdot \overline{u(t-\tau)u(t-\tau_1) \ldots u(t-\tau_i)} \mathrm{d}\tau_1 \ldots \mathrm{d}\tau_i \\ =& \sum_{i=1}^{\infty}\int_0^T \ldots \int_0^T g_i(\tau_1, \ldots, \tau_i) \cdot R_{u \ldots u}(\tau_1 - \tau, \ldots, \tau_i - \tau) \mathrm{d}\tau_1 \ldots \mathrm{d}\tau_i. \end{aligned} \tag{3.30}$$

Now, let's introduce one of the properties of the m-sequences, the so-called shift and add property [34]. It arises from the method of how they are generated using the LFSR. When we take any m-sequence and multiply it by the same but shifted sequence, we obtain the same sequence, but with a different time shift. For example, with the sequence $u[n]$ having a length of 15 chips

$$\begin{aligned} u[n] =& [\circ\circ\circ\circ\bullet\circ\bullet\circ\circ\bullet\bullet\circ\bullet\bullet\bullet] \\ \cdot u[n-1] =& [\bullet\circ\circ\circ\circ\bullet\circ\bullet\circ\circ\bullet\bullet\circ\bullet\bullet] \\ \hline = u[n-4] =& [\circ\bullet\bullet\bullet\circ\circ\circ\circ\bullet\circ\bullet\circ\circ\bullet\bullet], \end{aligned} \tag{3.31}$$

where the -1 and 1 numbers are for better illustration represented by $\circ$ and $\bullet$ symbols, respectively. It can be clearly seen that the original sequence multiplied by the same sequence

but shifted by one chip to the right equals the same sequence but shifted by 4 chips to the right. The shifts are unique for every m-sequence and can be determined from the feedback connections of the generating LFSR (or from the generating polynomial) of the m-sequence. Based on this property, it is now obvious that the second and higher order autocorrelation function of the m-sequence can be expressed as

$$R_{u...u}[\tau_1, \ldots, \tau_i] = \begin{cases} 1 & \text{under certain values of } \tau_1, \ldots, \tau_i \\ -\frac{1}{N} & \text{otherwise.} \end{cases} \tag{3.32}$$

For better illustration, the second order autocorrelation function of the very same m-sequence, which was used in previous examples, is depicted in Fig. 3.4. Its slices of third order autocorrelation function are depicted in Fig. 3.5.

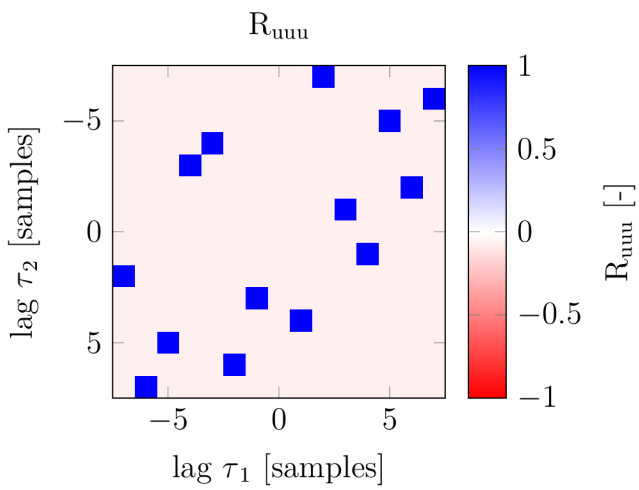

Fig. 3.4: Second order circular autocorrelation function of m-sequence.

Based on those observations, Eq. 3.30 then can be approximated, using Eq. 3.15 and taking into account only the first, second and third order Volterra kernels, which is a basic commonly used approximation, as

$$\begin{aligned} R_{yu}(\tau) \approx & \Delta t g_1(\tau) + F_3(\tau) \\ & +2! \sum_{j=1}^{m_2} (\Delta t)^2 g_2(\tau - k_{21}^{(j)} \Delta t, \tau - k_{22}^{(j)} \Delta t) \\ & +3! \sum_{j=1}^{m_3} (\Delta t)^3 g_3(\tau - k_{31}^{(j)} \Delta t, \tau - k_{32}^{(j)} \Delta t, \tau - k_{33}^{(j)} \Delta t), \end{aligned} \tag{3.33}$$

where the integers $k_{ir}^{(j)} (1 \leq r \leq i)$ are the unique shift coefficients of the m-sequence which can be derived from the generating polynomial of the sequence or can be observed on the high order autocorrelation functions drawings, m_i is the count of the sets of numbers $k_{ir}^{(j)}$. The constants 2! and 3! emerges from the symmetry of the higher order autocorrelation functions.

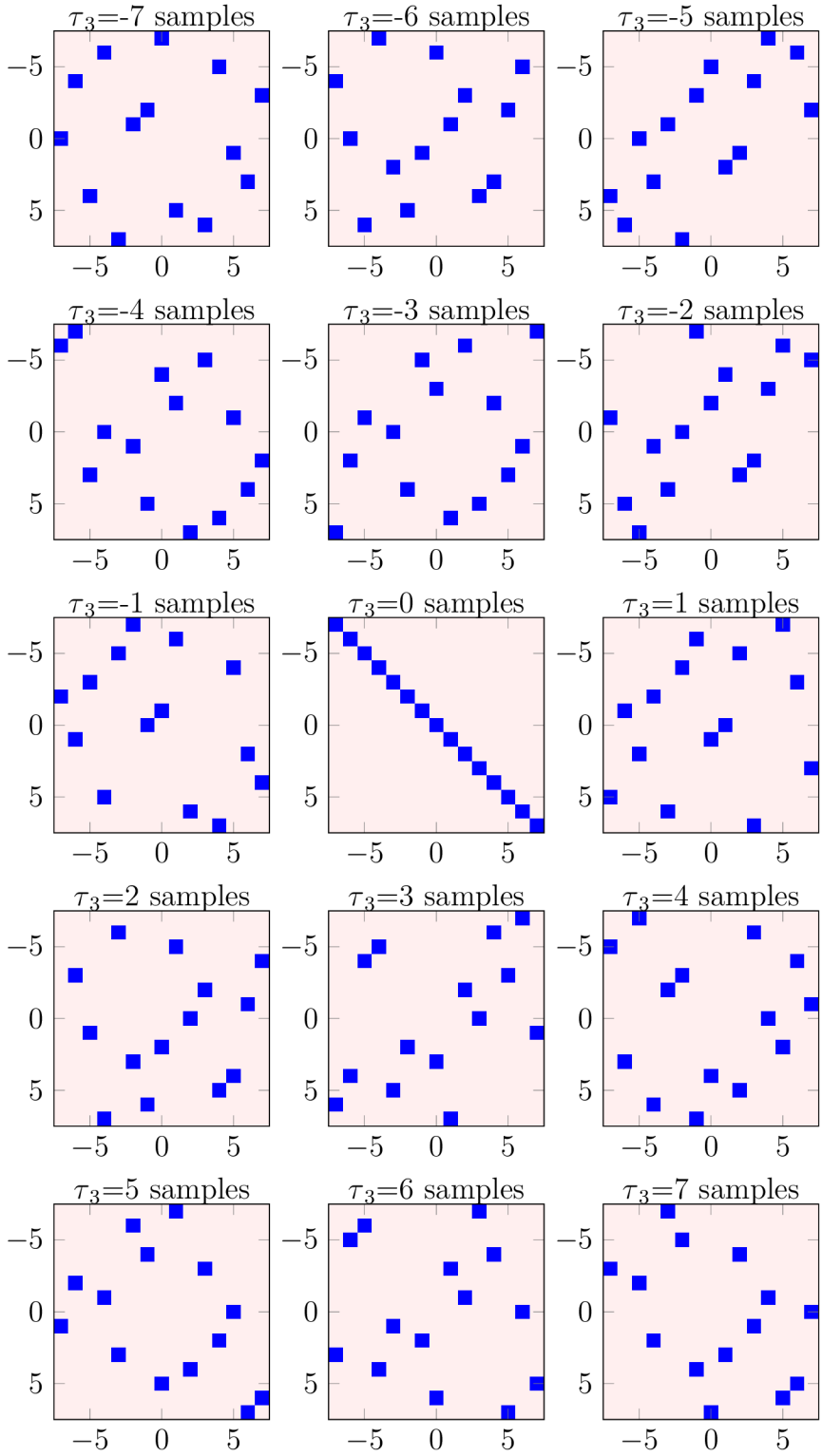

Fig. 3.5: Third order circular autocorrelation function of m-sequence.

We can observe that the cross-correlation now contains the first order kernel (linear impulse response) and also shifted cross sections of higher order kernels. The term $F_3(\tau)$ is the sum of

the third order Volterra kernels which have one or more parameters the same and equals to

$$F_3(\tau) = (\Delta t)^3 g_3(\tau, \tau, \tau) + 3(\Delta t)^3 \sum_{q=1}^{m_1} g_3(\tau, q, q). \tag{3.34}$$

3.4.1 Unobservable and overlapped kernels

As can be seen, there are several parts of the Volterra kernels that are not directly observable or are overlapped with other kernels.

In the concrete, we cannot observe any second order Volterra kernel which has an equal parameter, e.g. $g_2(q, q)$. This is because when the binary m-sequence is multiplied by the same m-sequence, the result is a constant 1, e.g. $u(t) \cdot u(t) = 1$ [35]. This can be generalized for all even order kernels but in the scope of this work, only kernels up to third order are considered.

From Eq. 3.34 we can see that any third order Volterra kernel, which have one or more parameters the same, overlaps with the first order kernel. The explanation is as follows: $u(t) \cdot u(t) \cdot u(t) = u(t)$ or more generally $u(t) \cdot u(t - \tau) \cdot u(t - \tau) = u(t)$. This property can also be generalized for all odd order kernels.

3.4.2 Mitigating the effects of even order kernels

It is possible to easily mitigate the effects of even order distortion by exploiting the property that

$$R_{(-u)\ldots(-u)}(\tau_1, \ldots, \tau_i) = \begin{cases} R_{u\ldots u}(\tau_1, \ldots, \tau_i) & \text{for odd } i \\ -R_{u\ldots u}(\tau_1, \ldots, \tau_i) & \text{for even } i. \end{cases} \tag{3.35}$$

The system is first probed by $u(t)$ and then by $-u(t)$. Outputs of the measurements (y_{pos} and y_{neg}, respectively) are then cross-correlated with their corresponding inputs and averaged to obtain an estimate of $g_1(\tau)$ which is not affected by even order distortion, e.g.

$$g_1(\tau) \approx \frac{1}{2\Delta t}(R_{y_{pos}u} + R_{y_{neg}(-u)}). \tag{3.36}$$

An example of such measurement is shown in Fig. 3.3 (b). The measurement setup is the same as in Fig. 3.3 (a). It can be clearly seen that the spurious peak located at 110 ns and some others have completely vanished. However, there are some others, for example that located at 8 ns, which remained because they were caused by odd order non-linear distortion. Nevertheless, the SFDR improved by 7.5 dB.

3.4.3 Golay complementary sequences as an input signal

Another great candidate for channel probing signal are the Golay complementary sequences pairs [36]. They are easily constructed by recursive algorithms and have a perfect (both aperiodic and periodic) autocorrelation function. A deeper description of Golay complementary

sequences is beyond the scope of this thesis, but to illustrate consider $a[n]$ and $b[n]$ complementary sequences of length 16 chips. Their circular autocorrelation functions are depicted in Fig. 3.6. An average (sum divided by two) of those autocorrelation functions is perfect, e.g.

Fig. 3.6: Circular autocorrelation functions of complementary pairs.

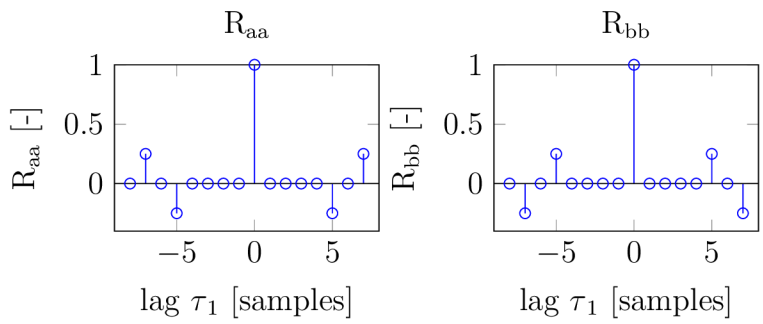

$$(R_{aa}[\tau_1] + R_{bb}[\tau_1])/2 = \begin{cases} 1 & \text{if } \tau_1 = 0 \\ 0 & \text{elsewhere.} \end{cases} \tag{3.37}$$

Averages of higher order autocorrelation functions of Golay complementary sequences have also interesting properties. For illustration, the second order autocorrelation function is depicted in Fig. 3.7 and the third order autocorrelation function in Fig. 3.8.

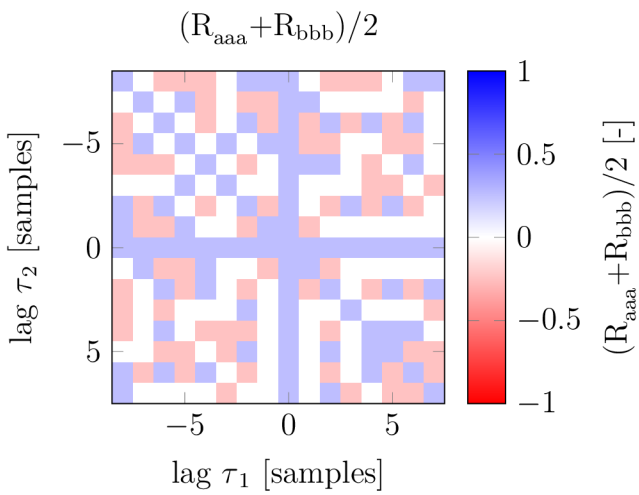

Fig. 3.7: Second order circular autocorrelation function of complementary Golay sequences.

As can be seen, the maximal value of those functions is lower than if m-sequences are used and it even gets lower for longer Golay complementary sequences. Some of the terms are negative and some are positive which can cause that some artefacts, caused by the non-linearities will cancel out. Also, those functions are more noise-like than in the case of m-sequences. That will cause that the artefacts will not appear as spurious peaks as in case of m-sequences, but will be spread over time and will increase the overall noise floor instead.

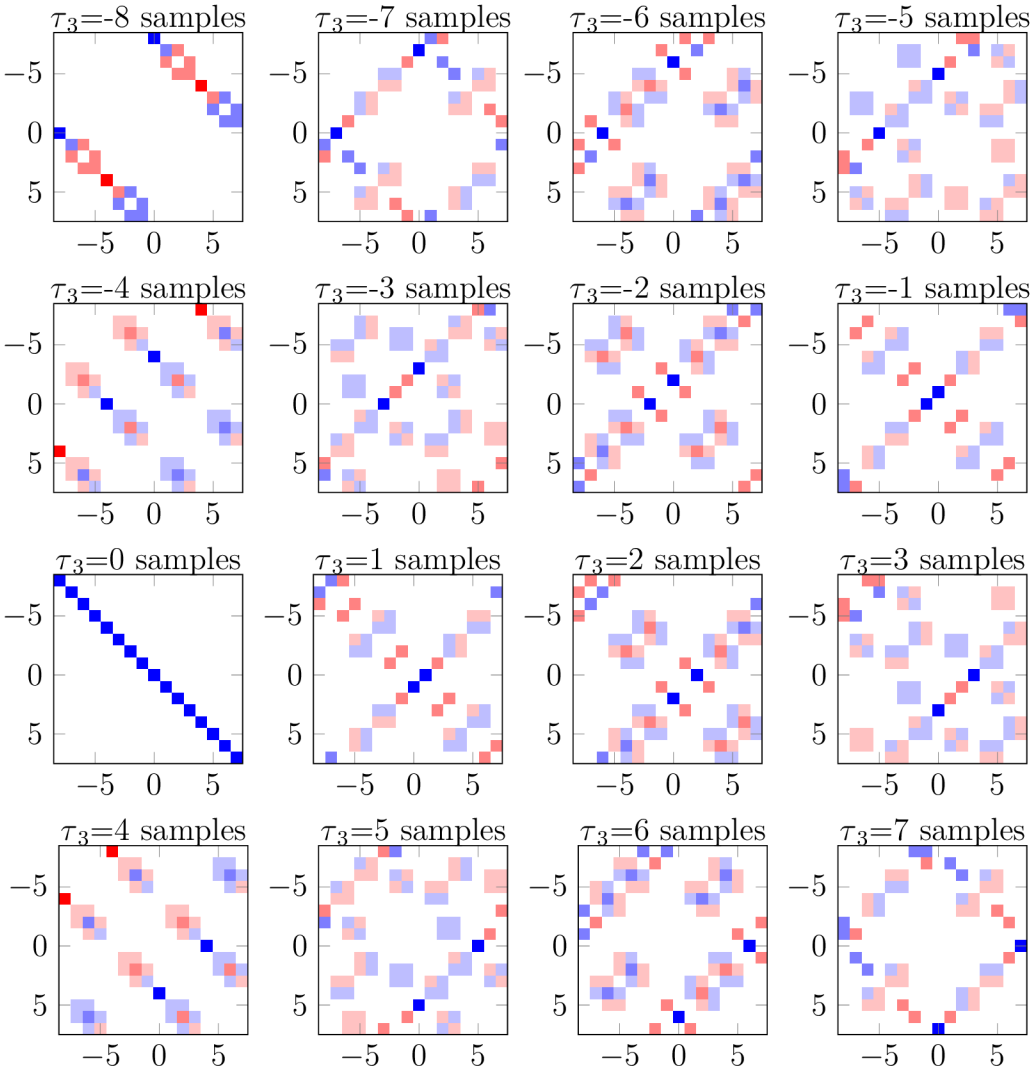

Fig. 3.8: Third order circular autocorrelation function of complementary Golay sequences.

An example measurement using Golay complementary sequences is depicted in Fig. 3.3 (c). There are practically no spurious peaks, but the overall noise floor is slightly higher as was explained in the previous paragraph. The SFDR has further improved by 12.3 dB. Nevertheless, the amplitude of the estimated impulse response is of course still affected by the non-linearities.

3.4.4 Non-inverted and inverted Golay complementary sequences as an input signal

It is also possible to apply the approach from Sec. 3.4.2 to the Golay complementary sequences. In this case, the system is probed by four sequences: $a(t)$, $-a(t)$, $b(t)$ and $-b(t)$. Outputs of the measurements are then cross-correlated with their corresponding inputs and averaged to

obtain an estimate of $g_1(\tau)$, which is not affected by even order distortion, e.g.

$$g_1(\tau) \approx \frac{1}{4\Delta t}(R_{y_{apos}a} + R_{y_{aneg}(-a)} + R_{y_{bpos}b} + R_{y_{bneg}(-b)}). \tag{3.38}$$

3.5 Probing the system with multiple sequences

When the system is probed with only one periodic sequence (for example with the m-sequence, as was shown earlier in Sec. 3), the process of obtaining the CIR at some time instant is straightforward. The sequence is seamlessly repeated at the transmitter and at the receiving side, it is possible to take a snapshot with a length of the sequence T at any time. The estimate of the CIR is then obtained by computing the (circular) cross-correlation between the transmitted and received signal (Eq. 3.25).

However, as was proven earlier, it is often more advantageous to probe the system with two or more sequences. This scenario is depicted in Fig. 3.9. In this example, four sequences $(a, -a, b, -b)$ are used. Every sequence is transmitted twice because the channel introduces some delay and in order to obtain a correct CIR estimate, it is needed that the receiving (correlation) window (of length T) contains only the corresponding sequence. This is illustrated in the example by a direct and delayed path. The signals from those paths are added at the receiver and the correlation windows are correctly aligned so that it contains only corresponding sequences.

This approach of course significantly extends the measurement time, during which the channel has to remain static. However, in our measurement scenarios, it is still possible to consider the channel static also for small multiples of T, thus it has a negligible effect on the CIR estimate.

It is also not necessary to repeat each sequence twice; it is possible to repeat only a fraction of the sequence as long as the length of the repeated section is larger than the maximal delay introduced by the channel. This approach is similar to the well known Cyclic Prefix (CP) which is used commonly in OFDM systems over fading channels. Using this technique, it is possible to adjust the overall signal (set of sequences) length to an arbitrary value. For example, in some of our measurement scenarios, the transmitter and receiver cannot be connected by a reference and triggering cable, so the triggering at the receiving side was performed based on the 10 MHz reference signal, generated locally by a Rubidium or Global Positioning System (GPS) disciplined oscillator. The overall signal length was adjusted to be an exact multiple of the period of this reference signal.

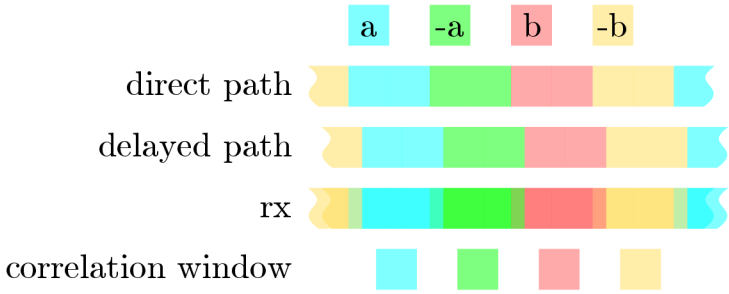

Fig. 3.9: Probing the system with multiple sequences.

3.6 SFDR of the system

3.6.1 SFDR of the baseband system

Results presented in this section were obtained by the back-to-back test of the baseband system, e.g. the output of the baseband binary sequence generator was connected directly to the oscilloscope by a coaxial cable.

The used baseband binary sequence generator offers variable output power from -19 dBm to 13 dBm. Probably due to the variable output amplifier stage, it has different signal purity at various output power levels. Four sets of sequences SFDR were measured and compared. Each sequence has approximately the same length (T), however, each set has a different count of sequences. Each sequence was transmitted twice for the reasons mentioned in the previous section. This, of course, results in different measurement times when using different sets of sequences. The sets with fewer sequences were repeated and averaged to improve the SNR and to provide an objective comparison in terms of measurement time. The used sets and their corresponding properties are summarized in Tab. 3.1. Measurement results are shown

Set name	# of sequences	Meas. time	Averaging factor
m-seq.	1	T	8
m-seq., inv. m-seq.	2	4T	2
Golay pair	2	4T	2
Golay pair, inv. Golay pair	4	8T	1

Tab. 3.1: Sets of sequences used for measurements.

in Fig. 3.10. To give a better insight into the performance of individual sets, results where several thousands of measurements were averaged, are also depicted. This helps to differentiate whether the SFDR is limited by the spurs or by noise.

It can be seen that the basic m-sequence has the lowest SFDR under all circumstances and that the SFDR is limited by spurious peaks at all power levels, thus cannot be improved by

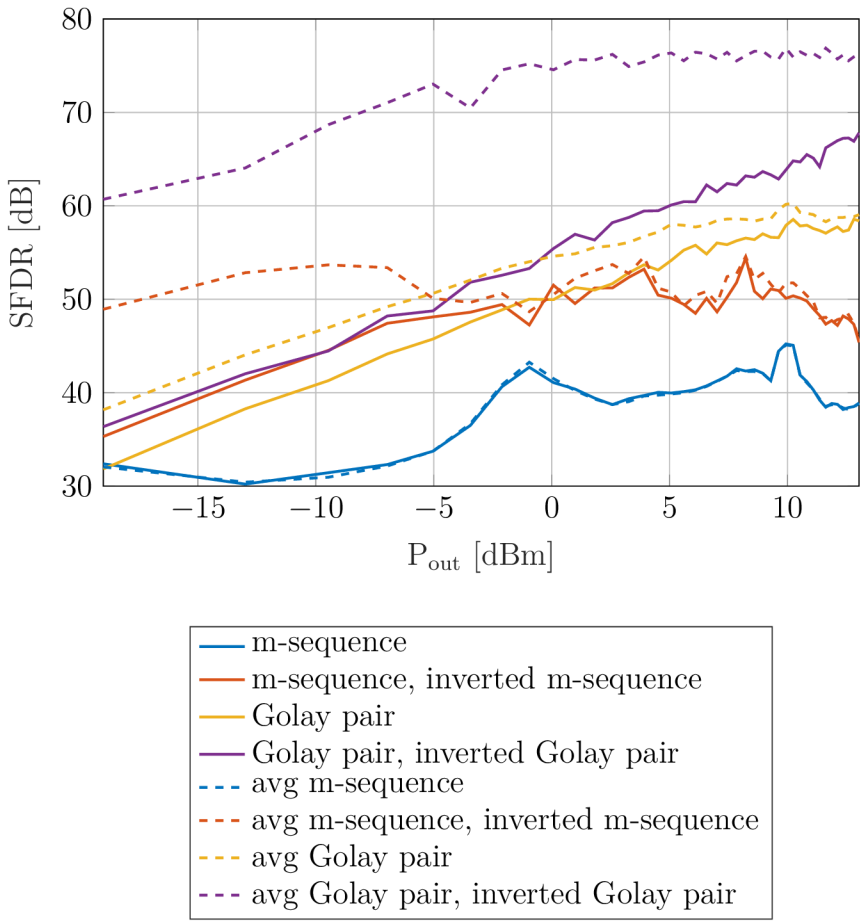

Fig. 3.10: SFDR of the baseband system.

averaging.

The m-sequence and inverted m-sequence performs better. Its SFDR is limited by the noise of the system to the output power level approximately -5 dBm and then it is limited by the spurs.

As was stated in the previous sections, the Golay complementary pairs behave differently. It can be seen that SFDR can be slightly improved by averaging at all power levels.

The combined approach of the Golay pairs and inverted Golay pairs, which completely mitigates the effects of the even order kernels and then exploits the Golay pairs' properties, shows superior performance under all circumstances.

3.6.2 SFDR of the system without PA and LNA

The results presented in this section were obtained by the back-to-back test of the system without amplifiers, e.g. the output of the up converter was connected directly to the input of the down converter by waveguides and coaxial cables.

Based on the results described in the previous section, the output level of the baseband

generator was set to 10 dBm, where the basic m-sequence has the best performance. This signal was then attenuated to match the input power level of the up converter and fed into its input.

A similar measurement as in the previous section was performed; this time varying the power level of the LO (of both up and down convertor) from 5 dBm to 14 dBm. The results are depicted in Fig. 3.11.

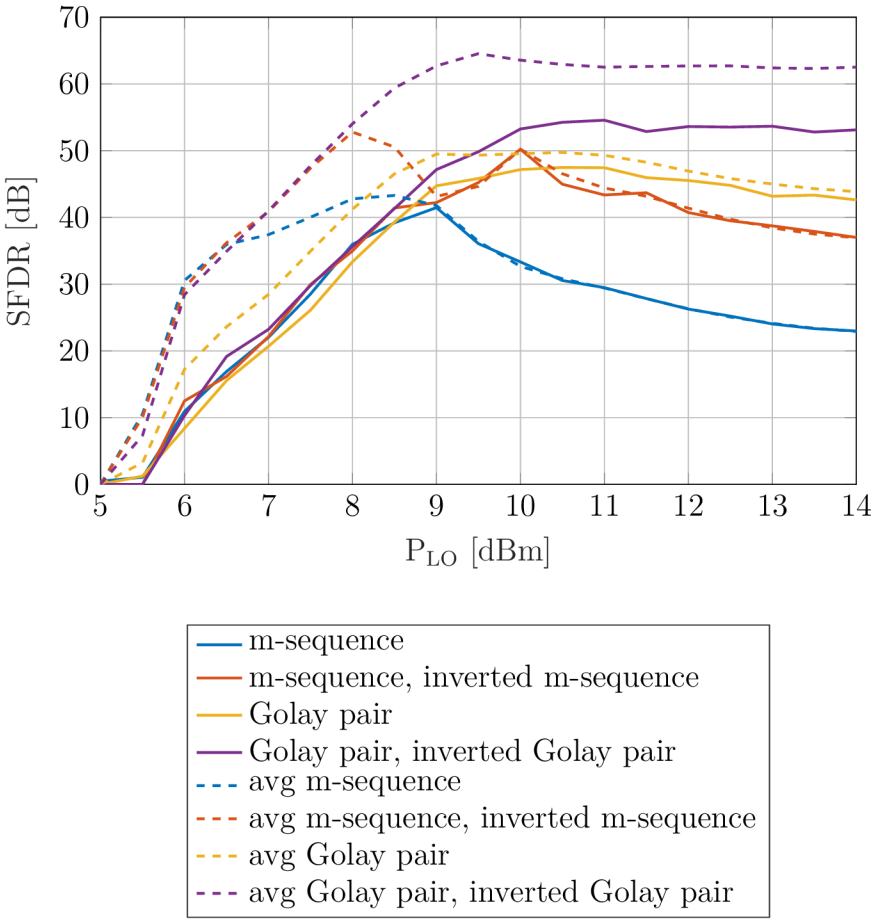

Fig. 3.11: SFDR of the system without PA and LNA.

The results are similar to the results carried out in the baseband. It can be seen that the up-down converter starts working at approximately 5 dBm of the LO input power. The SFDR (of all sets of sequences) increases until the power of approximately 9 dBm, where the up-down converter reaches saturation.

The SFDR of the two sets — m-sequence and m-sequence, inverted sequence — in the saturation is limited by the spurs and thus cannot be increased by averaging.

3.6.3 SFDR of the complete system (including PA and LNA)

The results presented in this section were obtained by the back-to-back test of the complete system which is depicted in Fig. 3.1. A variable attenuator was connected between the PA and LNA to simulate the path loss.

Based on the results described in the previous section, the LO power level was set to 9 dBm, where the basic m-sequence shows the best performance. The SFDR performance of all sets of sequences when varying the simulated path attenuation is depicted in Fig. 3.12.

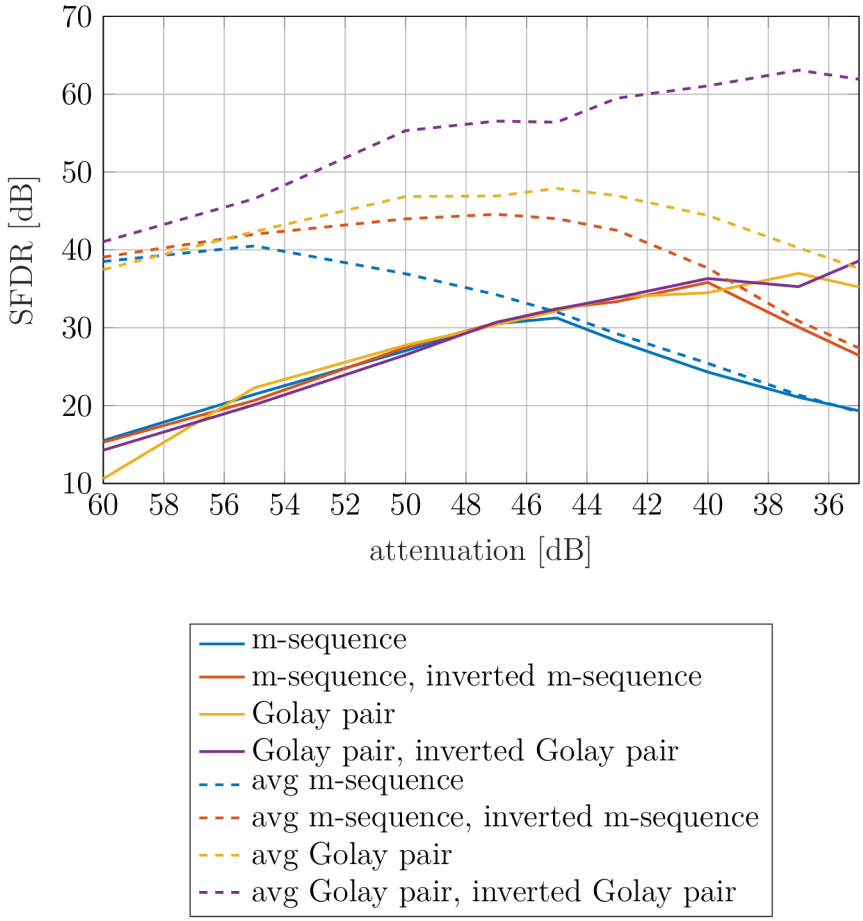

Fig. 3.12: SFDR of the complete system.

It can be seen that the performance of the system is limited mainly by the noise of the LNA. For this reason, the SFDR of all sets of sequences is almost the same at attenuation levels from 60 dB to 45 dB. At 45 dB of attenuation, the SFDR of the basic m-sequence starts to decrease as a result of the LNA non-linearity. The m-sequence and inverted m-sequence performs better, however, at 40 dB of attenuation, the performance starts to degrade as well.

The remaining two sets show increasing SFDR performance, however, at 35 dB of attenuation, the LNA reaches its 1 dB compression point, so it is inappropriate to increase the power level even more. This leads to maximal SFDR of approximately 40 dB. The averaged results

also show that the SFDR can be greatly increased by averaging, however, this impractically extends the measurement time.

3.7 IQ imbalance

The Sivers IMA FC1003V/01 [24] up-down converter, which is utilized in the system, uses a direct conversion (homodyne) architecture. This architecture offers several benefits, such as easy integration, low cost and high selectivity. On the other hand, it suffers from IQ amplitude and phase imbalance. Due to the huge bandwidth of the system, those imbalances are also frequency selective. Detailed discussion on the IQ imbalances issue can be found for example in [37].

This section describes a technique for frequency selective IQ imbalance estimation and compensation for the discussed channel sounder system. A similar system, including its (frequency flat) IQ imbalance calibration utilizing a delay line, was described in [9]. Approach described in this section can be done without any additional hardware (delay line) and compensates for frequency selective IQ imbalance.

As was stated earlier, only one of the IQ inputs is used in the up-converter at the transmitter side, thus the IQ imbalance is a concern only at the receiver side.

In scope of this section, we assume that the non-linear effects are mitigated by the techniques described in the previous section. Thus, we can consider $h(t) \approx g_1(t)$ and $H(f) \approx G_1(f)$. In this case, a single measured CTF, affected by the IQ imbalances, can be modeled as

$$H_i'(f) = H_i(f) + k(f) \cdot H_i(-f), \tag{3.39}$$

where $i = 1, 2, \ldots, N$ denotes the ith measurement in the set of N measurements, $H_i'(f)$ is the complex baseband representation of the CTF, $H_i(f)$ is the complex baseband representation of the CTF without the effects caused by IQ imbalance and $k(f)$ is the complex frequency dependent IQ imbalance coefficient.

Please note that the described channel sounder system operates in the time domain, e.g. the result of the measurement is the CIR. However, it is easy to transform between the time and frequency domain representation utilizing the FFT and IFFT, e.g.

$$H_i(f) = \mathrm{FFT}\{h_i(t)\} \tag{3.40}$$

and

$$h_i(t) = \mathrm{IFFT}\{H_i(f)\}. \tag{3.41}$$

As can be observed from Eq. 3.39, the IQ imbalance causes self-interference, which can be, depending on the phase shift between the transmitter and receiver, constructive or destructive.

To illustrate the situation, consider this scenario: the transmitter is connected directly to the receiver by a coaxial cable and attenuator (back-to-back) and one of the LOs has a small

frequency offset of $\Delta f \approx 100$ mHz. Several hundreds of CIRs are then taken at $f_{meas} \approx 10$ Hz. The resulting CIRs are depicted in Fig. 3.13.

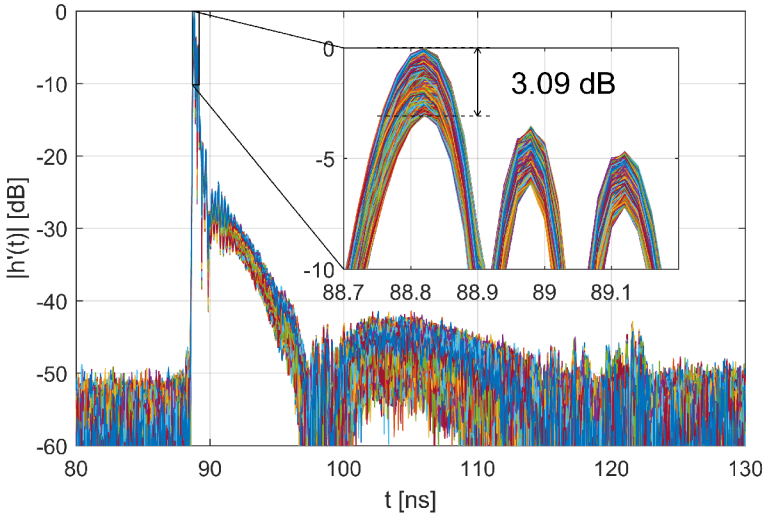

Fig. 3.13: Example of a back-to-back measurement without IQ imbalance correction.

As can be seen, there is one strong delayed path with decay, which corresponds to the behavior of a coaxial cable, however the amplitude of the strongest path varies by 3.09 dB within the observations, despite a completely static channel.

A trace of the strongest component of the CIR from Fig. 3.13, plotted in the complex plane, is depicted in Fig. 3.14, blue plot.

It can be clearly seen that the trace rotates around the origin according to the phase difference of the oscillators. However, it does not rotate around a perfect circle (green trace) but follows an elliptic curve, which is caused by the IQ imbalance. It also explains the amplitude fluctuation in Fig. 3.13 — ellipse does not have a constant distance from the origin, which is the amplitude of the component.

3.7.1 IQ imbalance compensation

According to Eq. 3.39, an estimate of the original CTF can be recovered by

$$\hat{H}_i(f) = H'_i(f) + k'(f) \cdot H'_i(-f), \tag{3.42}$$

where $k'(f)$ is the complex correction coefficient.

The dataset (transformed into the frequency domain), depicted in Fig. 3.13, can be considered as a calibration data in order to obtain the correction coefficients $k'(f)$ as

$$k'(f) = \arg\min_{k' \in \mathbb{C}} \sigma^2(|H'(f) + k'(f) \cdot H'(-f)|), \tag{3.43}$$

where $\sigma^2(x)$ stands for the variance of the vector x and $H'(f) = [H'_1(f)\ H'_2(f)\ \ldots\ H'_N(f)]^T$. Using Eq. 3.43 for every frequency bin f, such value of $k'(f)$ can be found that the resulting

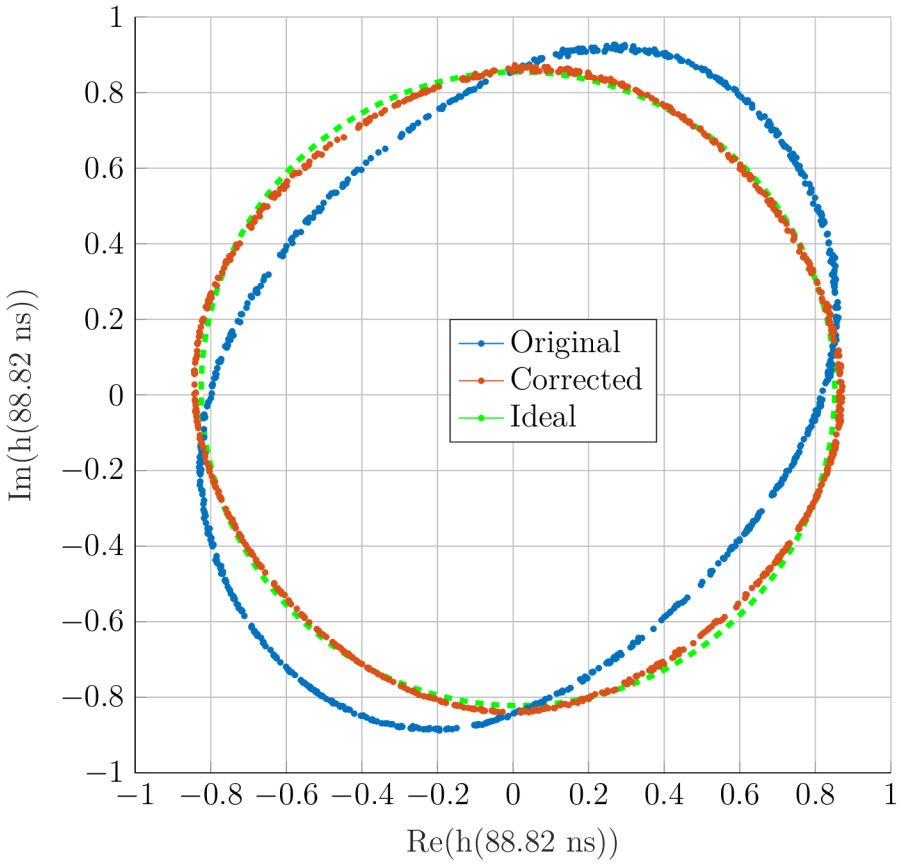

Fig. 3.14: Trace of the strongest component of the CIR in the complex plane. Blue: measured data, without IQ imbalance corrections, red: measured data, with IQ imbalance corrections, green: ideal (circle fit).

trace of $\hat{H}(f)$ in the complex plane fits a circle best in the least squares sense. The solution can be obtained iteratively by using MATLAB function FMINSEARCH.

Correction coefficient $k'(f)$, computed from the data shown in Fig. 3.13, utilizing Eq. 3.43, is depicted in Fig. 3.15. It can be seen that the absolute maximal value is about 0.3 at low frequencies and then it tends to reduce for higher frequencies, while the argument is almost constant for the whole frequency range. Please note that the used up-down converters have DC-coupled inputs and outputs, so there is no relevant information at near zero frequencies, which causes the spikes around 0 Hz. Also, as the absolute value of the correction coefficient $k'(f)$ is almost zero at higher frequencies, its argument is getting noisy.

Data from Fig. 3.13 with IQ imbalance corrections from Fig. 3.15 applied are depicted in Fig. 3.16. It can be seen that the amplitude fluctuation has reduced from 3.09 dB to 0.75 dB, e.g. by 2.34 dB. A trace of the strongest component of the IQ corrected CIR from Fig. 3.16, plotted in the complex plane, is depicted in Fig. 3.14, red plot. It can be seen that the shape approaches the ideal circle (green plot).

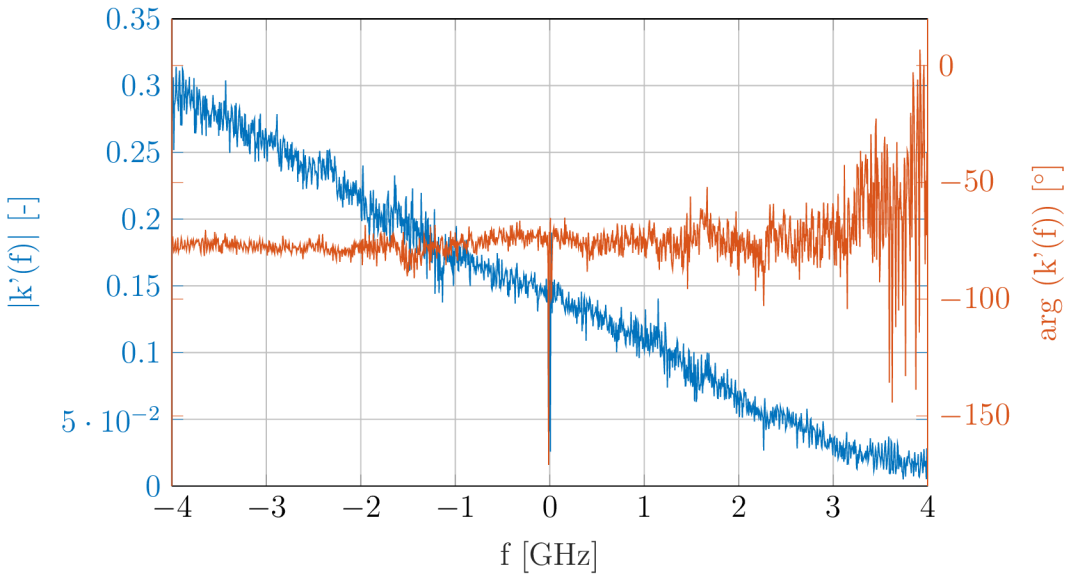

Fig. 3.15: Correction coefficient $k'(f)$, computed from data depicted in Fig. 3.13, in polar representation.

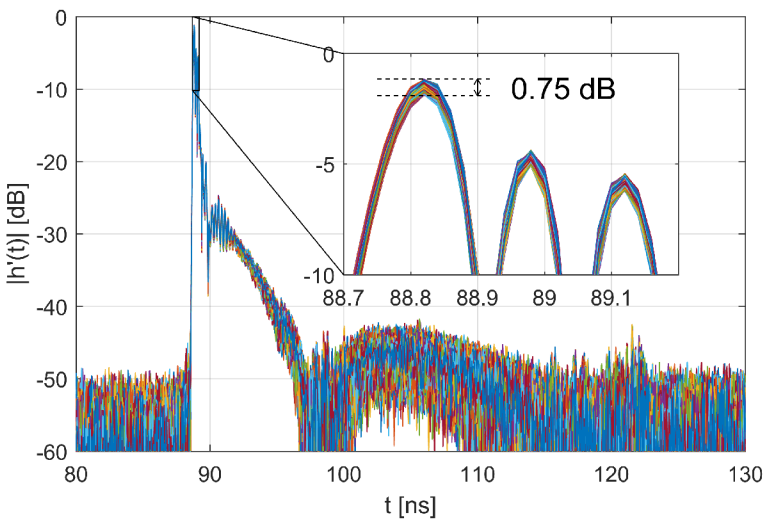

Fig. 3.16: Example of a back-to-back measurement with IQ imbalance correction.

4 CONCLUSION

This thesis dealt with the problem of measuring the fast varying and diverse MMW automotive channels. After brief introduction, the current channel measuring techniques, which are typically not able to capture all of the MMW channel features, were presented in Chapter 1. The goals were set in Chapter 2. Chapter 3 represented the core of the dissertation — it fulfilled the primary goal of building a channel sounding system suitable for the MMW channels. It thoroughly explains the development of the system, its hardware, methods, data processing, features and parameters. Great part of this chapter was dedicated to mitigating an issue, which arose during the system development. The dynamic range of the system was considerably limited by the spurs, that appeared in the measurement output. It turned out that it was caused by the non-linear components in the measurement chain and was significantly reduced by a careful analysis and choice of the probing signal. It was shown that the Golay pair and Golay pair with inverted polarity as probing signal exhibit superior performance in most of the cases. This was analysed and explained also theoretically exploiting signal properties such as higher order autocorrelation function.

To summarize, both of the goals set in Chapter 2 were accomplished. A measurement system with unique parameters (the primary goal) was built and presented in Chapter 3. Fulfillment of the secondary goal — actual measurements of various scenarios with the developed system — is included only in the full version of the dissertation.

BIBLIOGRAPHY

[1] A. Chandra, J. Blumenstein, T. Mikulasek, J. Vychodil, M. Pospisil, R. Marsalek, A. Prokes, T. Zemen, and C. Mecklenbrauker, "CLEAN algorithms for intra-vehicular time-domain UWB channel sounding," in *Proceedings of the 5th International Conference on Pervasive and Embedded Computing and Communication Systems*. SCITEPRESS - Science and and Technology Publications, 2015-2-11, pp. 224–229. [Online]. Available: http://www.scitepress.org/DigitalLibrary/Link.aspx?doi=10.5220/0005323702240229

[2] A. Chandra, J. Blumenstein, T. Mikulášek, J. Vychodil, R. Maršálek, A. Prokeš, T. Zemen, and C. F. Mecklenbräuker, "Serial subtractive deconvolution algorithms for time-domain ultra wide band in-vehicle channel sounding," *IET Intelligent Transport Systems*, vol. 9, no. 9, pp. 870–880, 2015. [Online]. Available: https://ietresearch.onlinelibrary.wiley.com/doi/abs/10.1049/iet-its.2014.0287

[3] J. Vychodil, A. Chandra, T. Mikulasek, A. Prokes, and V. Derbek, "UWB time domain channel sounder," in *Proceedings of 25th International Conference RADIOELEKTRONIKA 2015*, 2015, pp. 268–271.

[4] A. Dezfooliyan and A. Weiner, "Evaluation of time domain propagation measurements of UWB systems using spread spectrum channel sounding," *Antennas and Propagation, IEEE Transactions on*, vol. 60, no. 10, pp. 4855–4865, Oct 2012.

[5] A. Durantini, W. Ciccognani, and D. Cassioli, "UWB propagation measurements by PN-sequence channel sounding," in *Communications, 2004 IEEE International Conference on*, vol. 6, June 2004, pp. 3414–3418 Vol.6.

[6] J. Keignart, C. Abou-Rjeily, C. Delaveaud, and N. Daniele, "UWB SIMO channel measurements and simulations," *Microwave Theory and Techniques, IEEE Transactions on*, vol. 54, no. 4, pp. 1812–1819, June 2006.

[7] J. Kivinen, "60-GHz wideband radio channel sounder," *IEEE Transactions on Instrumentation and Measurement*, vol. 56, no. 5, pp. 1831–1838, Oct 2007.

[8] S. Guillouard, G. E. Zein, and J. Citerne, "High time domain resolution indoor channel sounder for the 60 GHz band," in *1998 28th European Microwave Conference*, vol. 2, Oct 1998, pp. 341–344.

[9] R. Zetik, M. Kmec, J. Sachs, and R. S. Thoma, "Real-time mimo channel sounder for emulation of distributed ultrawideband systems," *International Journal of Antennas and Propagation*, vol. 2014, p. 16, 2014. [Online]. Available: http://dx.doi.org/10.1155/2014/317683

[10] S. Ranvier, J. Kivinen, and P. Vainikainen, "Millimeter-wave MIMO radio channel sounder," *IEEE Transactions on Instrumentation and Measurement*, vol. 56, no. 3, pp. 1018–1024, June 2007.

[11] M. Schack, J. Jemai, R. Piesiewicz, R. Geise, I. Schmidt, and T. Kurner, "Measurements and analysis of an in-car UWB channel," in *Vehicular Technology Conference, 2008. VTC Spring 2008. IEEE*, May 2008, pp. 459–463.

[12] M. Schack, M. Jacob, and T. Kurner, "Comparison of in-car UWB and 60 GHz channel measurements," in *Antennas and Propagation (EuCAP), 2010 Proceedings of the Fourth European Conference on*, April 2010, pp. 1–5.

[13] K. Leechaikitjaroen, S. Promwong, P. Supanakoon, S. Chensirikul, and S. Kaewmechai, "Indoor measurement results of UWB impulse radio for shot-range wireless systems with RMS delay spread and path loss," in *Communications and Information Technology, 2005. ISCIT 2005. IEEE International Symposium on*, vol. 1, Oct 2005, pp. 684–688.

[14] L. Liu, Y. Wang, N. Zhang, and Y. Zhang, "UWB channel measurement and modeling for the intra-vehicle environments," in *Communication Technology (ICCT), 2010 12th IEEE International Conference on*, Nov 2010, pp. 381–384.

[15] J. Blumenstein, A. Prokes, A. Chandra, T. Mikulasek, R. Marsalek, T. Zemen, and C. Mecklenbraeuker, "In-vehicle channel measurement, characterization and spatial consistency comparison of 3-11 GHz and 55-65 GHz frequency bands," *IEEE Transactions on Vehicular Technology*, vol. PP, no. 99, pp. 1–1, 2016.

[16] E. Zochmann, C. F. Mecklenbräuker, M. Lerch, S. Pratschner, M. Hofer, D. Löschenbrand, J. Blumenstein, S. Sangodoyin, G. Artner, S. Caban, T. Zemen, A. Prokeš, M. Rupp, and A. F. Molisch, "Measured delay and doppler profiles of overtaking vehicles at 60 ghz," in *12th European Conference on Antennas and Propagation (EuCAP 2018)*, 2018, pp. 1–5.

[17] G. R. MacCartney and T. S. Rappaport, "A flexible millimeter-wave channel sounder with absolute timing," *IEEE Journal on Selected Areas in Communications*, vol. 35, no. 6, pp. 1402–1418, 2017.

[18] G. R. MacCartney, H. Yan, S. Sun, and T. S. Rappaport, "A flexible wideband millimeter-wave channel sounder with local area and nlos to los transition measurements," in *2017 IEEE International Conference on Communications (ICC)*, 2017, pp. 1–7.

[19] E. Ben-Dor, T. Rappaport, Y. Qiao, and S. Lauffenburger, "Millimeter-wave 60 GHz outdoor and vehicle AOA propagation measurements using a broadband channel sounder," in *Global Telecommunications Conference (GLOBECOM 2011), 2011 IEEE*, Dec 2011, pp. 1–6.

[20] C. Anderson, T. Rappaport, K. Bae, A. Verstak, N. Ramakrishnan, W. Tranter, C. Shaffer, and L. Watson, "In-building wideband multipath characteristics at 2.5 and 60 ghz," in *Proceedings IEEE 56th Vehicular Technology Conference*, vol. 1, 2002, pp. 97–101 vol.1.

[21] D. Ferreira, R. F. Caldeirinha, and N. Leonor, "Real-time high-resolution radio frequency channel sounder based on the sliding correlation principle," *IET Microwaves, Antennas & Propagation*, vol. 9, no. 8, pp. 837–846, 2015. [Online]. Available: https://ietresearch.onlinelibrary.wiley.com/doi/abs/10.1049/iet-map.2014.0165

[22] E. Lemos Cid, M. Garcia Sanchez, and A. Vazquez Alejos, "High speed transmission at 60 ghz for 5g communications," in *2015 IEEE International Symposium on Antennas and Propagation USNC/URSI National Radio Science Meeting*, 2015, pp. 1007–1008.

[23] R. Müller, R. Herrmann, D. A. Dupleich, C. Schneider, and R. S. Thomä, "Ultrawideband multichannel sounding for mm-wave," in *The 8th European Conference on Antennas and Propagation (EuCAP 2014)*, 2014, pp. 817–821.

[24] *FC1003V/01 V-band Converter*, Sivers IMA AB. [Online]. Available: http://siversima.com/wp-content/uploads/FC1003V01-Data-Sheet.pdf

[25] T. Mikulasek, J. Blumenstein, and A. Prokes, "Antennas utilized for intra-vehicle 3-11 GHz and 55-65 GHz channel measurement," in *2016 Progress in Electromagnetic Research Symposium (PIERS)*, Aug 2016, pp. 4258–4262.

[26] *FC1005V/00 V-band Converter*, Sivers IMA AB. [Online]. Available: http://siversima.com/wp-content/uploads/FC1005V00-Data-Sheet.pdf

[27] C. Chen, *Signal Processing Handbook*, ser. Electrical and Computer Engineering. New York: Taylor & Francis, 1988. [Online]. Available: https://books.google.cz/books?id=10Pi0MRbaOYC

[28] J. McLaughlin and J. Raviv, "Nth-order autocorrelations in pattern recognition," *Information and Control*, vol. 12, no. 2, pp. 121 – 142, 1968. [Online]. Available: http://www.sciencedirect.com/science/article/pii/S0019995868902416

[29] L. G. Weiss, "Wavelets and wideband correlation processing," *IEEE Signal Processing Magazine*, vol. 11, no. 1, pp. 13–32, Jan 1994.

[30] G. Gong, F. Huo, and Y. Yang, "Large zero autocorrelation zones of Golay sequences and their applications," *IEEE Transactions on Communications*, vol. 61, no. 9, pp. 3967–3979, September 2013.

[31] H. Harada, Y. Toyozawa, M. Shigaki, H. Kashiwagi, and T. Yamaguchi, "Identification of nonlinear parameters by using m-sequence and harmonic probing method," *Journal of System Design and Dynamics*, vol. 2, no. 1, pp. 209–217, 2008.

[32] V. Kekatos, D. Angelosante, and G. B. Giannakis, "Sparsity-aware estimation of nonlinear volterra kernels," in *Computational Advances in Multi-Sensor Adaptive Processing (CAMSAP), 2009 3rd IEEE International Workshop on*, Dec 2009, pp. 129–132.

[33] H. Tsukino, H. Harada, Y. Toyozawa, H. Kashiwagi, and R. Ohtsubo, "Identification of nonlinear parameters by using low-pass filtered M-sequence," in *ICCAS-SICE, 2009*, Aug 2009, pp. 4512–4515.

[34] Y. Lin, "Shift and add property of m-sequences and its application to channel characterisation of digital magnetic recording," *IEEE Proceedings - Communications*, vol. 142, no. 3, pp. 135–140, Jun 1995.

[35] E. Nishiyama, "Identification of first order volterra kernels of m-sequence correlation method for nonlinear system," in *Control, Automation and Systems, 2007. ICCAS '07. International Conference on*, Oct 2007, pp. 939–942.

[36] V. Braun, "Dipulse-response measurement of a magnetic recording channel using golay complementary sequences," *IEEE Transactions on Magnetics*, vol. 34, no. 1, pp. 309–316, Jan 1998.

[37] M. Valkama, M. Renfors, and V. Koivunen, "Advanced methods for I/Q imbalance compensation in communication receivers," *Signal Processing, IEEE Transactions on*, vol. 49, no. 10, pp. 2335–2344, Oct 2001.

ABSTRACT

This doctoral thesis deals with the millimeter wave band wireless channel measurement techniques in automotive applications. After a brief introduction into the topic and the summary of the current channel measurement techniques, the goals — the development and assembly of a measurement system, capable of capturing all of the millimeter wave band channel features and practical measurements with this system, are set. The next part is the core of the dissertation — the developed channel sounder is presented and a detailed description of used methods, principles, hardware and data processing is given. A significant part of the thesis is dedicated to the mitigation of the unwanted effects caused by the non-linear components in the measurement chain. Practical measurements of various scenarios — the intra-car channels, vehicle to vehicle channels as well as vehicle to infrastructure channels — are included only in the full version of the dissertation.

KEYWORDS

millimeter wave band, channel impulse response, channel sounding, m-sequences, Golay sequences, non-linearities

ABSTRAKT

Tato disertační práce se zabývá metodami měření přenosových kanálů v pásmu milimetrových vln se zaměřením na automobilové aplikace. Po stručném úvodu do problematiky a shrnutí současných metod měření přenosových kanálů jsou vytyčeny cíle práce — návrh a sestavení měřícího systému, schopného zachytit všechny rysy a detaily rychle se měnícího únikového přenosového kanálu a praktická měření s tímto systémem. Následuje jádro disertace — představení vyvinutého systému a detailní popis použitých metod, principů, hardwaru i způsob zpracování naměřených dat. Podstatná část práce je věnována eliminaci nechtěných jevů, způsobených nelineárními prvky v systému. Výsledky praktických měření různorodých scénářů — kanálů pro komunikaci uvnitř vozidla, mezi vozidly i mezi vozidly a infrastrukturou — jsou popsány pouze v plné verzi disertace.

KLÍČOVÁ SLOVA

milimetrové vlny, impulsní odezva kanálu, měření impulsní odezvy kanálu, m-sekvence, Golay sekvence, nelinearity

VYCHODIL, Josef *Millimeter wave band wireless channel measurement techniques in automotive applications*: short version of doctoral thesis. Brno: Brno University of Technology, Faculty of Electrical Engineering and Communication, Department of Radio Electronics, 2021. 37 p. Supervised by Dr. Techn. Vojtěch Derbek